SOIL FAILURE MODELS FOR VERTICALLY OPERATING AND HORIZONTALLY OPERATING STRENGTH SENSORS

S. O. Chung, K. A. Sudduth

ABSTRACT. *Soil strength, or mechanical resistance of a soil to failure, has been widely used to estimate the degree of soil compaction. Conventional measurements with cone penetrometers are laborious; therefore, an on-the-go soil strength profile sensor that collects data dense enough to show the spatial within-field variability in soil strength would be a desirable alternative. Because soil failure involves complex interactions among many variables, determining design parameters of a soil strength sensor and interpreting test results could be improved with a theoretical understanding of the soil failure process. Mathematical models to estimate the force required to penetrate (cut and displace) soil with a prismatic cutter traveling horizontally and with a cone penetrometer traveling vertically were developed based on the passive earth pressure theory and the concept of a variable failure boundary. Both models were expressed as additive forms of density, cohesion, and adhesion components of the soil, with each effect multiplied by a corresponding dimensionless number. Charts of dimensionless numbers were developed to investigate the behavior of each strength component at various values of soil internal friction angle, soil-metal friction angle, and tool cutting angle. The models were used in simulation to optimize design parameters of the sensor, including component dimensions and the location and spacing of sensing elements. Based on this optimization, a prismatic sensing tip with a 3.61 cm^2 base area and a 60° cutting angle was selected, and the corresponding simulated maximum force and strength measurements were 2.2 kN and 6.0 MPa when operating at speeds up to 5 m s^{-1}. Model validation showed that the extension of the failure boundary was significantly correlated with soil properties such as bulk density, water content, and internal friction angle. The variable failure boundary model developed in this study more consistently and accurately represented field data than did three previously developed modeling approaches.*

Keywords. *Penetrometers, Precision agriculture, Sensors, Soil compaction, Soil strength.*

Concern about soil compaction has increased as agricultural machinery has become larger and tillage practices have changed in recent decades. Compaction, which increases soil strength and decreases soil aeration, can restrict the growth of plant roots and negatively affect the environment (Hillel, 1980; Soane and Van Ouwerkerk, 1995). Because direct field measurements of compaction are difficult, soil strength is often used as a surrogate measurement (Canarache, 1991), with the cone penetrometer (*ASAE Standards*, 2003a, 2003b) being the primary measurement device. However, cone penetrometer readings are discrete point measurements, making it difficult to collect enough data to accurately represent within-field variations in soil strength. A soil strength sensor able to obtain measurements at multiple depths continuously while traveling across the field would be much more efficient in detecting compacted zones, and several such prototype sensors have been developed (e.g., Glancey et al., 1989; Adamchuk et al., 2001; Andrade et al., 2001; Chukwu and Bowers, 2005).

After reviewing the advantages and disadvantages of each existing sensor, we initiated a project to address the problem with a somewhat different design, beginning with a theoretical understanding of soil failure processes. The variables involved in soil failure interact with each other in a complex manner. Because of this, determining design parameters of a sensor and interpreting test results on the basis of experimental results alone would be difficult. Mathematical modeling and simulation could reduce the number of experiments required and give a better understanding of test results. Knowledge of the relationships between soil strength and the controlling factors, potentially obtained from simulation, is also important for proper application of the sensor measurements. Another use of soil failure modeling would be to theoretically compare on-the-go sensor results with data obtained using a cone penetrometer.

Tools working in soil exert forces that cause different soil failure patterns corresponding to stress-strain behaviors: tension, compression, shear, and plastic flow. Several mathematical force prediction models for narrow tines and soil-penetrating tools have been developed using the passive earth pressure theory developed by Rankine (Gill and Vanden Berg, 1968). Payne (1956) applied theories of classical soil mechanics to investigate the performance of soil implements. In the case of wide tools, he neglected the edge effects of the tool in describing draft since the aspect ratio

Submitted for review in March 2005 as manuscript number PM 5823; approved for publication by the Power & Machinery Division of ASABE in June 2006. Presented at the 2003 ASAE Annual Meeting as Paper No. 031028.

The authors are **Sun-Ok Chung, ASABE Member Engineer,** Agricultural Engineering Researcher, National Institute of Agricultural Engineering, Rural Development Administration, Suwon, Republic of Korea; and **Kenneth A. Sudduth, ASABE Member Engineer,** Agricultural Engineer, USDA-ARS Cropping Systems and Water Quality Research Unit, University of Missouri, Columbia, Missouri. **Corresponding author:** Kenneth A. Sudduth, 269 Agricultural Engineering Bldg., University of Missouri, Columbia, MO 65211; phone: 573-882-4090; fax: 573-882-1115; e-mail: sudduthk@missouri.edu.

(depth/width) was small, reducing the problem to a two-dimensional case. Later, Hettiaratchi et al. (1966) used the logarithmic spiral method in their two-dimensional analysis to determine passive earth pressure. Their model included terms accounting for cohesive, adhesive, frictional, and gravitational forces.

The assumption that edge effects are negligible is not valid for the case of narrow tools. For narrow tines, Payne (1956) observed that the bottom surface of cleavage would be interrupted by side surfaces, and a block of soil adjacent to the tine would be isolated. He also stated that narrow tines would not displace the soil far enough laterally to bring it into plastic equilibrium. Several three-dimensional mathematical models have been developed to predict draft force and the soil area disturbed by a narrow tine: Hettiaratchi and Reece (1967), Godwin and Spoor (1977), and McKyes and Ali (1977).

As in the case of narrow tines, several models have been proposed based on the soil failure patterns around a vertically operating tip (Terzaghi, 1943; Meyerhof, 1951; Hu, 1965). Godwin and Spoor (1977) used Meyerhof's approach to derive a force model for lateral soil failure (or flow failure) caused by a horizontally operating prismatic cutter. Gill and Vanden Berg (1968) stated that total force on a prismatic cutter could be separated into normal force and tangential forces on the wedge of the cutter, and tangential force on the side of the cutter. Alihamsyah et al. (1990) tested a horizontally operating penetrometer using conical and prismatic tips. With a prismatic tip, soil penetration resistance was reduced since the tip displaced soil only to the sides.

This theoretical analysis was part of an overall project to design and evaluate a prototype on-the-go soil strength profile sensor. The purpose of the sensor was to obtain "CI-like" measurements at multiple depths directly in front of a soil-cutting tool as it traveled across a field at speeds near those of normal tillage operations, and to detect spatial and vertical variability of soil strength under field conditions. Results of previous investigations (e.g., Alihamsyah et al., 1990) led to our choice of a prismatic tip as a horizontally moving, soil-penetrating tool to minimize interference between the tips at different depths.

Objectives

The overall objective of this research was to model soil failure caused by prismatic and conical tools and to conduct model simulations to obtain information useful for sensor design and the interpretation of test results. Specific objectives were to:

- Develop and validate mathematical models of soil failure caused by a horizontally operating prismatic tool (i.e., soil strength profile sensor, SSPS) and a vertically operating conical tool (i.e., cone penetrometer).
- Investigate the relationships between soil strength and controlling factors, and between the soil strength index measured by the soil strength profile sensor and cone index (CI) measured by the cone penetrometer.
- Determine parameters and considerations for sensor design, such as the expected range of soil strength and the effects of tool geometry on measured forces.

Model Development

Prior Research

Factors affecting soil failure caused by a tool can be identified by the equations in analytical models (e.g., Gill and Vanden Berg, 1968; Hettiaratchi and Reece, 1974; Plasse et al., 1985), a semi-empirical technique like the dimensional analysis method (e.g., Schuring and Emori, 1964; Wismer and Luth, 1972), or experimental study (e.g., Alihamsyah et al., 1990). The parameters generally fall into four categories: (1) tool design: lengths and angles describing tool geometry, and interaction between elements due to arrangement; (2) soil conditions: unit weight, internal friction, cohesion, clay content, particle size distribution, water content, and organic matter content; (3) soil-tool interactions: soil-tool friction and adhesion, and (4) operating conditions: operating depth and speed. These factors, as well as interactions between the factors, influence soil failure behavior in a complex manner.

Soil shear failure has been analyzed and explained using the Mohr-Coulomb failure theory. Based on the Mohr-Coulomb theory, the location of soil failure can be found if the shape of the soil failure surface is known. Unfortunately, this shape is not known in most cases. Experimental observations have found soil failure surfaces to be formed of combinations of a curved line near the tool and a straight line connecting the curve and ground surface (e.g., Payne, 1956). This logarithmic spiral method has been used to estimate soil failure surfaces in modeling of soil movement by tines

Table 1. Variable notations, definitions, and measurement units.

Notation	Definition and Units
α	Cutting angle of the tool, $\pi - 2\varepsilon$ (radians)
β	Extension of radial shear zone (radians)
δ	Soil-tool friction angle (radians)
ε	Base angle of the tool (radians)
ϕ	Soil internal friction angle (radians)
γ	Unit weight of soil (N m^{-3})
η	$0.25\pi - 0.5\phi$ (radians)
θ	$0.75\pi + 0.5\phi - \varepsilon + \beta$ (radians)
b	Width of the tool (m)
c	Cohesion of soil (N m^{-2})
c_a	Adhesion of soil to the tool (N m^{-2})
D	Operating depth of a prismatic tip (m)
e	Base of natural logarithms
F	Force acting on the tool (N). Subscripts: p (prismatic tool), c (conical tool), and i (inertia)
g	Acceleration of gravity (9.81 m s^{-2})
h	Height of a prismatic tip (m)
m	Unit mass of soil (kg m^{-3})
N	Dimensionless number describing geometry of the soil failure. Subscripts: p (prismatic tool), c (conical tool), γ (soil weight), c (cohesion), and a (adhesion)
p_0	Geostatic pressure due to soil weight (N m^{-2})
q_f	Average unit pressure acting on the shaft (N m^{-2})
q_n	Normal component of the passive pressure acting on the tool base (N m^{-2})
r_0, r_1	Radii of the logarithmic spiral at $w = 0$ and θ, respectively (m)
s, p	Shear and normal stress (N m^{-2})
t	Time (s)
v	Speed of the tool (m s^{-1})
w	Angle of the logarithmic spiral (radians)
W	Weight of soil acting on the failure zone (N)
z	Operating depth of the tool (m)

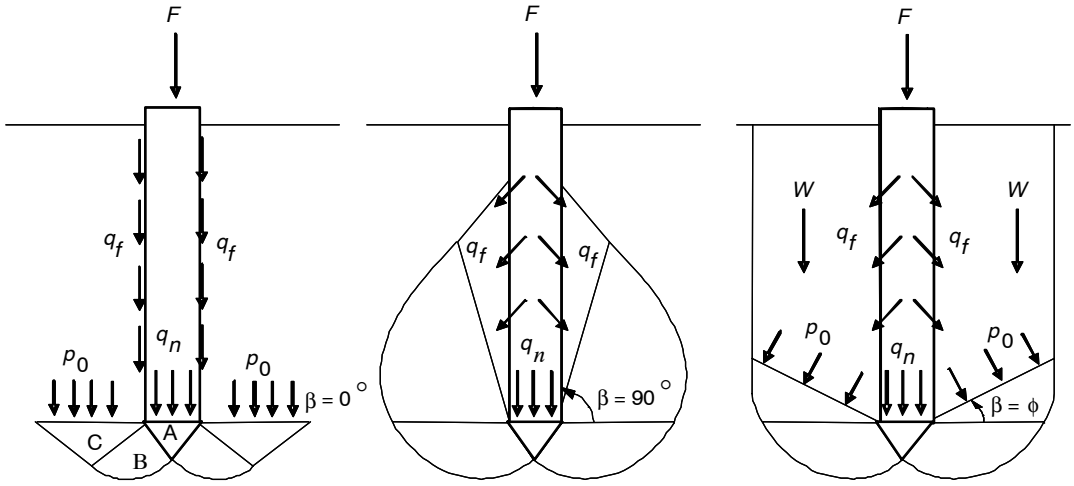

Figure 1. Patterns of soil failure under deep foundations as proposed by Terzaghi (1943, left), Meyerhof (1951, center), and Hu (1965, right).

(e.g., Terzaghi, 1943; Osman, 1964) and bearing capacity of foundations by soil-penetrating bodies (e.g., Terzaghi, 1943; Meyerhof, 1951; Hu, 1965). Using the variable notations given in table 1, the equation for a logarithmic spiral is:

$$r = r_0 e^{w \tan \phi} \quad (1)$$

Models of soil failure due to a horizontally operating prismatic tool and a vertically operating conical tool in a homogeneous soil can be derived using theories developed for soil movement by narrow tines and the bearing capacity of foundations. Figure 1 shows three variations of the soil failure pattern, as assumed by previous researchers. The soil failure boundary (fig. 1, left) proposed by Terzaghi (1943) consisted of a wedge-shaped central zone (A), two zones of radial shear (B), and two passive Rankine zones of plane shear (C). For a shallow foundation, the shearing resistance of the soil located above the level of the foundation base was neglected and replaced by pressure acting at the level of the base.

Meyerhof (1951) argued that observed soil movement was not in accordance with the above failure mechanism, especially in a cohesive material with internal friction, and extended the zone of radial shear so that the failure area increased with foundation depth (fig. 1, center). For shallow depths, results of laboratory and field tests on buried and driven foundations in clay and sand showed good agreement with the theory. For deep foundations, however, actual base resistance was less than estimated and an empirical compressibility factor was introduced to reduce the shearing strength.

To overcome limitations of Meyerhof's model in frictional soils and for deep foundations, Hu (1965) limited the zone of radial shear to the area where the lateral distance of the failure zone from the shaft was a maximum, and took the effect of soil weight (*W*) above the failure zone into account in the calculation of base resistance (fig. 1, right). Theoretical values showed good agreement when compared with experimental results for the base resistance of buried strip foundations in loose and dense sand. However, for cohesive soils, the estimated resistance needed to be corrected with a depth-dependent factor greater than 1.

Although the general formulation of these three models was similar, they differed in definition of the radial shear zone. These variations in approach were attempts to accurately model the soil failure behavior for different soils, due to the fact that a single failure model would not fit to actual resistance data collected under different soil (e.g., cohesion, internal friction, texture, compressibility, bulk density, and water content), tool, and operational conditions. In this research, we developed a more general model based on those of Terzaghi (1943), Meyerhof (1951), and Hu (1965) by defining the extension of the radial shear zone as a variable (β). Our new "variable failure" model was a generalization of the above three models, which could be obtained by setting β to 0°, 90°, and ϕ °, respectively.

Horizontally Operating Prismatic Tool

Using the Mohr-Coulomb criteria, the soil failure surface will be the one that results in the minimum total force on a soil-penetrating body. The minimum force can be obtained by varying the location of the origin of the log spiral curves (Osman, 1964). Hettiaratchi et al. (1966) showed that curves of individual force functions were flat in the vicinity of their minimum turning points, and the minimum force was similar to the value when the origin of the log spiral was at the outside edge of the tool base. Therefore, for simplicity of computation, a close approximation was obtained by setting the origin of the log spiral at the outside edge of the base of the penetrating body, or point *a* in figure 2. We used ideal soil failure with a combination of log spirals and straight lines for force modeling. However, we used continuous log spirals to evaluate the distance of soil disturbance and the inertia effect due to operating speed, to maintain the continuity of the failure surface seen in real soils (fig. 2), as suggested by Godwin and Spoor (1977). The continuous log spiral was obtained by setting β = ϕ, where the lateral distance of the failure zone from the shaft was a maximum.

In a study modeling the cleavage of soil by tined implements, O'Callaghan and Farrelly (1964) stated that a vertical tine showed two modes of rupture determined by the aspect ratio (depth/width) of the tine. The transition from one mode to the other occurred when the aspect ratio was 0.6 for a flat vertical tine. O'Callaghan and McCoy (1965) extended the work to cleavage of soil by inclined and wedge-shaped tines. They found that the mode of cleavage was similar for both flat and wedge-shaped tines and that raking a tine

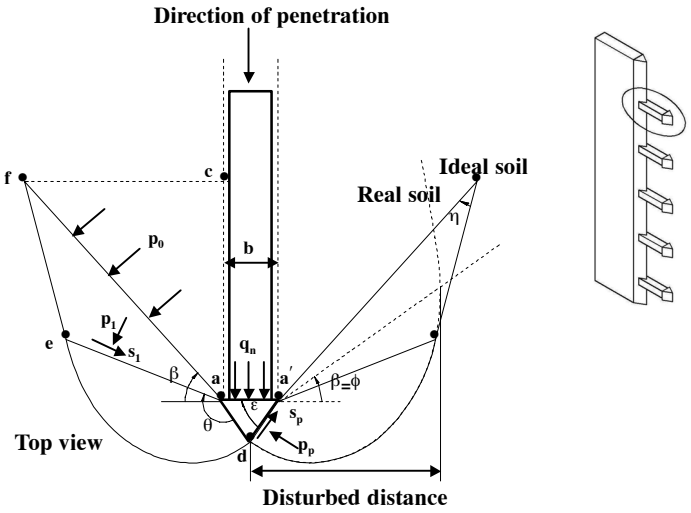

Figure 2. Soil failure mechanism for a horizontally operating prismatic tool, assuming only lateral failure. Inset shows location of prismatic tool (circled) as part of a multiple-depth soil strength sensor.

forward in the travel direction increased the depth of mode transition (critical depth). Godwin and Spoor (1977) identified two failure mechanisms: an upper failure zone near the ground surface where the soil displacement had forward, sideways, and upward components (crescent failure), and a lower failure zone where the displaced soil had only forward and sideways components (lateral failure). They showed that, with a flat vertical tine of 25.4 mm width, lateral failure occurred at depths lower than about 120 mm (aspect ratio $\geq$4.7). In this study, we assumed that only lateral failure occurred along the entire operating depth since the prismatic tool was wedge-shaped, vertical, and narrow. Crescent failure was assumed to occur only very near the ground surface, and therefore the possibility of crescent failure was not included in the model.

The soil strength that a horizontally operating prismatic tool (i.e., soil strength profile sensor) will encounter can be derived from the normal component of the passive pressure acting on the tool base, as described by equation A.8 in the Appendix. A prismatic tool likely displaces the soil only in the lateral direction, so the prediction of soil strength becomes a simple problem by neglecting edge effects of the tool in the upper and lower vertical directions. The only effect of soil weight is the geostatic pressure acting along the line *af*, the magnitude of which is $p_0 = \gamma z(1 - \sin\phi)$ (Lambe and Whitman, 1969). The effect of shaft friction through the area *acf* was not added to the geostatic pressure since the cross-sectional area of the shaft was assumed to be smaller than the base area of the tip. Integrating equation A.8 over the length *ad* ($b/(2\cos\varepsilon)$) and depth (z) gives the corresponding normal force (F_{ps}) acting on the prismatic tool in a static or quasi-static condition:

$$\begin{aligned} F_{ps} &= \gamma b z^2 \left[\frac{\cos^2\phi\cos(\varepsilon-\delta)}{2\cos\varepsilon\cos\delta} e^{2\theta\tan\phi} \right] \\ &\quad + cbz \left[\frac{\cot\phi\cos(\varepsilon-\delta)}{\cos\varepsilon\cos\delta} \left\{ (1+\sin\phi)e^{2\theta\tan\phi} - 1 \right\} \right] \\ &\quad + c_a bz\tan\varepsilon \\ &= \gamma b z^2 N_{ps\gamma} + cbzN_{psc} + c_a bzN_{psa} \end{aligned} \qquad (2)$$

High speeds near those encountered in normal tillage operations may result in a significant force increase. McKyes (1985) discussed two dynamic effects: inertia forces due to accelerating the soil volume, and changes in soil strength at a high rate of shear. He also stated that the effect of shear rate was not significant in purely frictional soils, but was significant in clay soils, outweighing the inertia forces. Stafford (1984) showed that there would be a large effect of strain rate on soil shear strength in "flow failure" of the soil, when no distinct shear planes were evident. He also stated that flow failure was likely to occur at high water content (above the plastic limit) or high speed. In our study, only inertia forces were taken into account, assuming no viscosity under normal tillage field conditions (e.g., Reece, 1965). Inertia forces can be calculated by integrating the soil volume being accelerated by a prismatic tool along the log spiral failure surface:

$$\begin{aligned} F_{pi} &= m\frac{v}{t} \\ &= \frac{2v\gamma xzb}{2tg} \left[\frac{e^{(\pi-\varepsilon+\phi)\tan\phi}}{\cos\varepsilon} + 1 \right] \\ &= \frac{\gamma z b v^2}{g} \left[\frac{e^{(\pi-\varepsilon+\phi)\tan\phi}}{\cos\varepsilon} + 1 \right] \end{aligned} \qquad (3)$$

Equations 2 and 3 are the forces acting on a prismatic tool when the height of the tool is equal to the operating depth. For a soil strength profile sensor that has multiple sensing tips at different depths, z in the equations needs to be evaluated from $D - 0.5h$ to $D + 0.5h$, where D and h are operating depth below the soil surface and height of each tip, respectively. Then, dividing the summation of the resultant forces by the base area gives the soil strength for the horizontally operating prismatic tool. The forces acting on an individual prismatic tip and corresponding prismatic soil strength index (PSSI) are:

$$F_{ps} = 2\gamma bhzN_{ps\gamma} + cbhN_{psc} + c_a bhN_{psa} \qquad (4)$$

$$F_{pi} = \frac{\gamma b h v^2}{g}\left[\frac{e^{(\pi-\varepsilon+\phi)\tan\phi}}{\cos\varepsilon}+1\right] \quad (5)$$

$$\text{PSSI} = \frac{F_{ps}+F_{pi}}{bh} \quad (6)$$

Vertically Operating Conical Tool

The force model for soil failure due to a vertically operating conical tool (fig. 3; i.e., cone penetrometer) was also derived from equation A.8. As in the case of a horizontally operating tool, the effect of shaft friction is ignored, due to the shaft being smaller than the conical tool as prescribed by ASAE standard S313.3 (*ASAE Standards*, 2003a). In the case of a vertical penetration, the maximum value of β is a function of operating depth (z) as given by equation 7 (adapted from Meyerhof, 1951). At shallow depths, β_{max} is constrained by equation 7 because the soil failure boundary may reach the ground surface before it is developed fully. At greater depths where the failure boundary can develop fully, β_{max} is π/2. Then, the value of θ is also a function of operating depth:

$$\beta_{\max} = \sin^{-1}\left(\frac{2\cos(\eta+\phi)\sin\eta}{b\cos\phi e^{\theta\tan\phi}}z\right) \quad (7)$$

The length of the plane shear surface *af* is also dependent on operating depth. Therefore, the average geostatic pressure (p_0) acting on the plane shear surface is given by equation 8:

$$p_0 = \gamma z\left(\cos\beta+(1-\sin\phi)\sin\beta\right)\times\left(1-\frac{be^{\theta\tan\phi}\cos\eta\sin\beta}{2z\cos\varepsilon}\right) \quad (8)$$

In the model for a horizontally operating tool, the only effect of soil weight was through the geostatic pressure acting on the plane shear surface. In case of a vertically operating tool, there was an additional effect of soil weight within the soil failure volume. The passive force due to the soil weight was found by balancing the moments about point *a′* (fig. 3). Forces considered in the equilibrium of moments were the resistance (P_1) due to the soil wedge *ge′f′*, the weight (W) of the segment *a′de′g*, and the passive force ($P\gamma$) acting normal to the cone surface (fig. 3). Detailed procedures of the force calculation were as explained by Osman (1964). The force component normal to the cone base per unit length of *a′d* was:

$$F_{cs\gamma'} = P_\gamma \frac{2\cos\varepsilon\cos(\varepsilon-\delta)}{b\cos\delta} \quad (9)$$

Integrating equations A.8 and 9 over the cone surface, $\pi b^2/(4\cos\varepsilon)$, and summing the resultant forces gives the corresponding normal force (F_{cs}) acting on a cone penetrometer in a static or quasi-static condition:

$$\begin{aligned} F_{cs} &= F_{cs\gamma} + F_{cs\gamma'} \\ &= \gamma b^2 z\left[\frac{\pi(1+\sin\phi)\cos(\varepsilon-\delta)}{4\cos\varepsilon\cos\delta}\right. \\ &\quad \times e^{2\theta\tan\phi}(\cos\beta+(1+\sin\phi)\sin\beta) \\ &\quad \left.\times\left(1-\frac{be^{\theta\tan\phi}\cos\eta\sin\beta}{2z\cos\varepsilon}\right)\right] \\ &\quad + \gamma b^3\left[\frac{P_\gamma\cos(\varepsilon-\delta)}{2\gamma b^2\cos\delta}\right] \\ &\quad + cb^2\left[\frac{\pi\cot\phi\cos(\varepsilon-\delta)}{4\cos\varepsilon\cos\delta}\left\{(1+\sin\phi)e^{2\theta\tan\phi}-1\right\}\right] \\ &\quad + c_a b^2\left[\frac{\pi\tan\varepsilon}{4}\right] \\ &= \gamma b^2 z N_{cs\gamma} + \gamma b^3 N_{cs\gamma'} + cb^2 N_{csc} + c_a b^2 N_{csa} \end{aligned} \quad (10)$$

Inertia forces on the conical tool can be calculated by modification of equation 3, as given by equation 11:

$$\begin{aligned} F_{ci} &= m\frac{v}{t} \\ &= \frac{v\gamma x\pi b^2}{4tg}\left[\frac{e^{(\pi-\varepsilon+\phi)\tan\phi}}{\cos\varepsilon}+1\right]^2 \\ &= \gamma b^2 v^2\frac{\pi}{4g}\left[\frac{e^{(\pi-\varepsilon+\phi)\tan\phi}}{\cos\varepsilon}+1\right]^2 \end{aligned} \quad (11)$$

Summing the forces in equations 10 and 11 and dividing by the base area of the cone gives the soil strength for the vertically operating conical tool, normally referred to as cone index (CI), and given by equation 12:

$$CI = \frac{F_{cs}+F_{ci}}{(\pi/4)b^2} \quad (12)$$

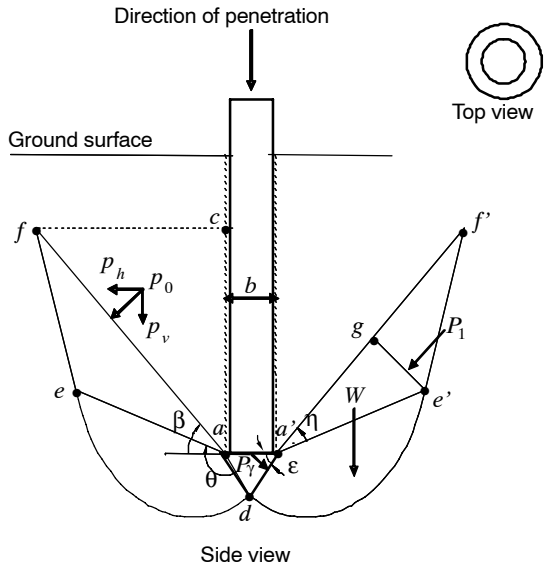

Figure 3. Soil failure mechanism for a vertically operating conical tool.

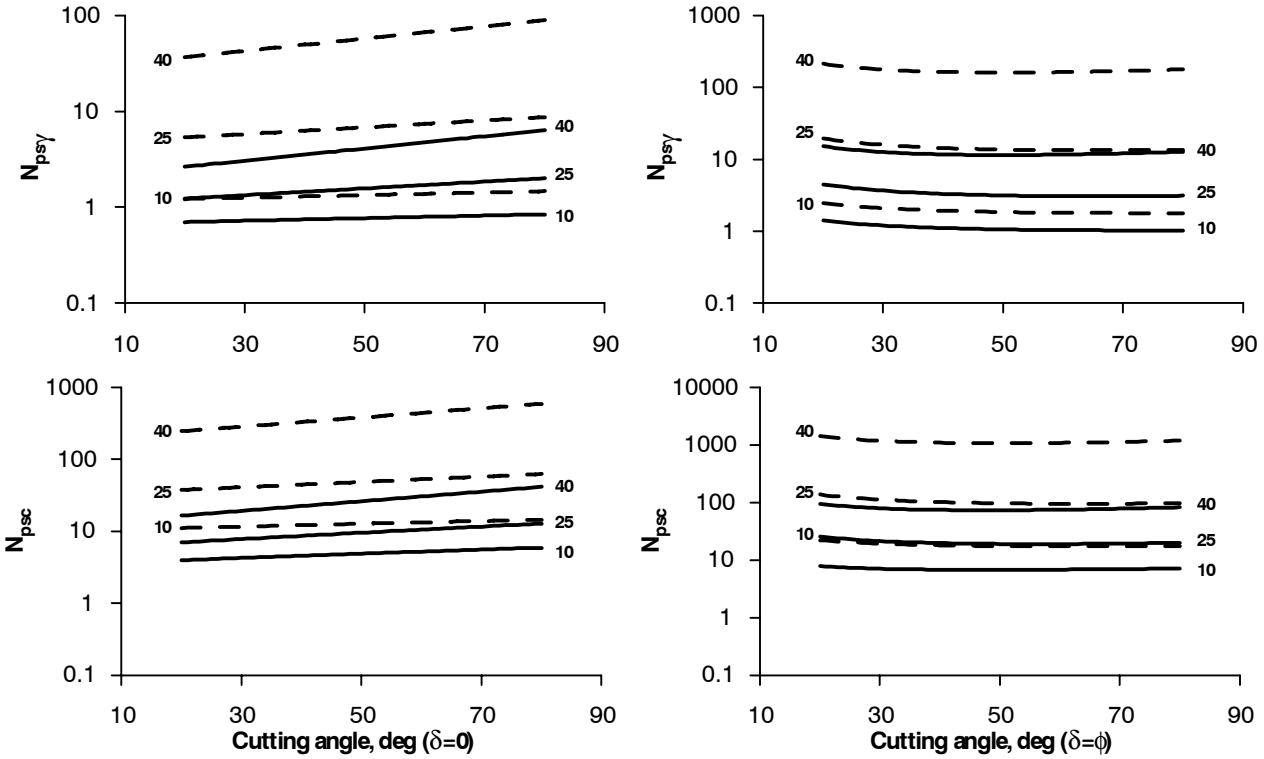

Figure 4. Changes in gravitational (top) and cohesive (bottom) dimensionless numbers for a horizontal prismatic cutter at different cutting angles, soil internal friction angles (10˚, 25˚, and 40˚, shown numerically in the graphs), soil-tool friction angles, and extensions of the shear zone (solid line, β = 0˚; dashed line, β = 90˚).

Model Characterization

Horizontally Operating Prismatic Tool

Soil strength measured by a horizontally operating prismatic tool would vary due to the many factors involved in the soil failure process, as described by equations 4 and 5. In equation 4, the resultant static passive force was expressed as additive terms of three force components (gravitational, cohesive, and adhesive pressure) multiplied by corresponding dimensionless numbers (N_{ps} γ, N_{psc}, and N_{psa}). Quantification of the force requires determination of the dimensionless numbers, which are functions of cutting angle, soil internal friction angle, and soil-tool friction angle, and reflect the shape of the soil failure region.

The first two dimensionless numbers in equation 4, the gravitational ($N_{ps}\gamma$) and cohesive (N_{psc}) components, determine a large portion of the resultant static force and include complex nonlinear terms. Figure 4 shows the behavior of the gravitational (top) and cohesive (bottom) dimensionless numbers at different cutting angles, soil internal friction angles, soil-tool friction angles, and extension angles of the radial shear zone. The cohesive dimensionless number was larger than the gravitational dimensionless number by a factor of 10. Both dimensionless numbers increased as the soil internal friction angle, soil-tool friction angle, and extension angle of the radial shear zone increased.

For a perfectly smooth surface (δ = 0), a sharper cutter (smaller cutting angle) resulted in a smaller value. However, for a perfectly rough surface (δ = ϕ), a minimum value did not occur at the smallest cutting angle but at intermediate or large angles. With δ = ϕ, the cutting angles that produced the smallest dimensionless number at 10˚, 25˚, and 40˚ soil internal friction angles were 80˚, 65˚, and 50˚ for the gravitational component ($N_{ps}\gamma$), and were 48˚, 56˚, and 48˚ at β = 0˚ and 63˚, 63˚, and 50˚ at β = 90˚ for the cohesive component (N_{psc}).

Vertically Operating Conical Tool

The forces acting on a vertically operating conical tool and the resulting soil failure patterns differ from those for a horizontally operating prismatic tool for two main reasons: different tip geometries (i.e., conical vs. prismatic), and the effects of geostatic pressure and soil weight due to the different operating directions (i.e., vertical vs. horizontal). Differences in the inertia component (eqs. 5 and 11) are only due to differences in tool geometry, i.e., surface area of the tip. The force in a quasi-static condition (eqs. 4 and 10) differs due to the effects of tool geometry and the direction of operation. The terms π/4 and π/2 in equation 10 account for the effects of the conical shape. The dimensionless number for the cohesive force on the tool base (N_{csc}) was identical to the corresponding term for the prismatic tool (eq. 4) except for these geometrical factors.

The effects of operating direction are more complex for a vertically operating conical tool. First, the geostatic pressure acting on the plane shear surface (p_0) and the limit of the radial shear zone (β_{max}) are functions of operating depth. Second, there is an additional gravitational component due to soil weight within the failure region. Figure 5 shows the behavior of the gravitational components due to geostatic pressure (top, $N_{cs}\gamma$) and weight of soil above the level of the conical tool base (bottom, $N_{cs}\gamma'$) at different cutting angles, soil internal friction angles, soil-metal friction angles, and

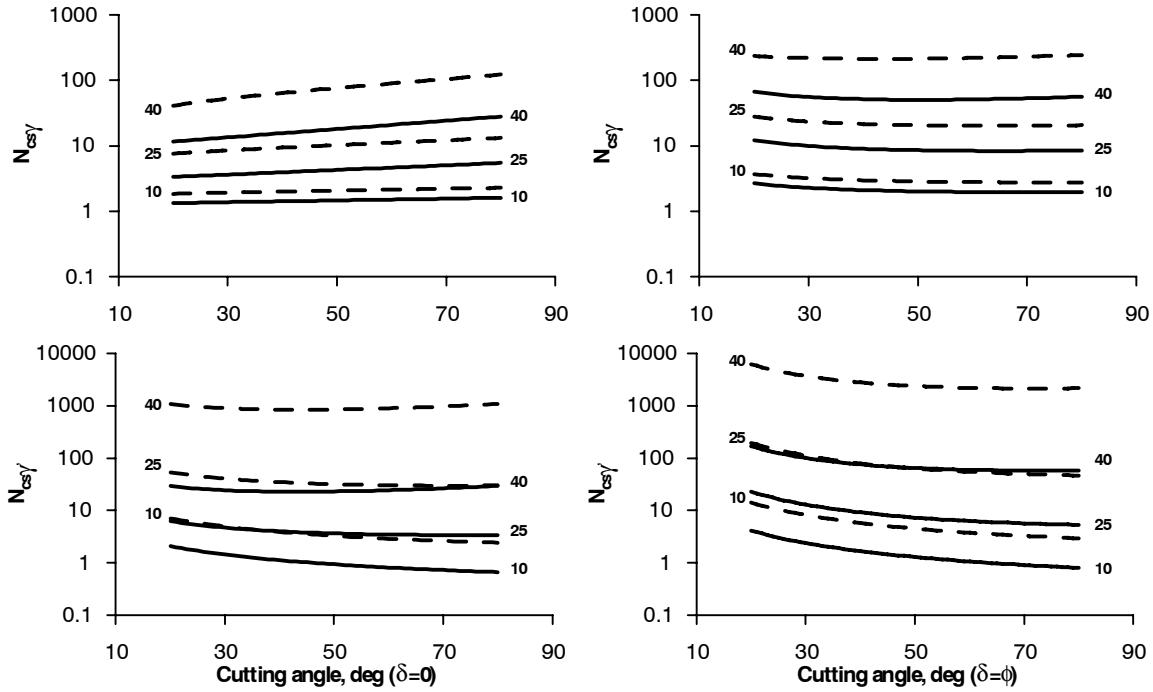

Figure 5. Changes in gravitational dimensionless numbers due to the geostatic pressure (top) and soil weight (bottom) for a vertical cone penetrometer at different cutting angles, soil internal friction angles (10°, 25°, and 40°, shown numerically in the graphs), soil-tool friction angles, and extensions of the shear zone (solid line, β = 0°; dashed line, β = 90°).

extension angles of the radial shear zone. In all cases, larger friction angles between soil particles resulted in larger forces on the tool, as was also seen for the horizontally operating prismatic tool. The gravitational dimensionless number for a vertically operating tool due to geostatic pressure showed values similar to those for a horizontally operating tool (compare top panels of figs. 4 and 5). The dimensionless number due to weight of soil within the failure volume ($N_{cs}\gamma$; fig. 5 top) was larger than the dimensionless number due to geostatic pressure ($N_{cs}\gamma'$; fig. 5 bottom) by a factor of 10.

Comparison of figures 4 and 5 indicates the influence of different aspects of the soil failure force components due to the different operating directions of the tools. Cohesive force was dominant for the horizontally operating tool, while gravitational force due to soil weight became significant along with cohesive force for the vertically operating tool. For a vertically operating tool, the geostatic pressure was a complicated function of both depth and extension angle of the radial shear zone, as compared to the simple form $\gamma z(1 - \sin\phi)$ for the horizontally operating tool. In addition, the effect of soil weight within the failure volume was greater than the effect of the cohesive component, especially for soils with larger soil-metal friction angles.

Applying the Model in Sensor Design

Simulations were performed with the model for a horizontally operating prismatic tool to determine several design parameters for an on-the-go soil strength profile sensor. Issues investigated were: (1) expected maximum soil strength to determine the required dynamic range of the sensor, (2) distance of soil disturbance to determine minimum spacing of the sensing tips, and (3) estimation of force profile as a function of operating depth.

We used results presented earlier in the Model Characterization section to select a cutting angle of 60º for the prismatic tip of the strength sensor. Because the cohesive component dominated the overall force on the horizontal prismatic cutter, and increased with increasing soil-tool friction angle, we wished to minimize N_{psc} at the maximum soil-tool friction angle ($\delta = \phi$). The 60º cutting angle provided close to the minimum cohesive force over a range of soil internal friction angles and radial shear zone extension angles (fig. 4).

Width and height of the cutting tip were both 1.9 cm, resulting in a 3.61 cm^2 base area, similar to the size of the ASAE-standard large penetrometer cone (3.23 cm^2) (*ASAE Standards*, 2003a, 2003b). Forces were evaluated to a depth of 0.5 m since this portion of the soil profile was considered to be important for the early stages of crop growth and because a large portion of the variability observed in CI data is typically contained within this depth (Chung and Sudduth, 2004; Chung, 2004).

For the simulation, extreme values from field tests described later in the Model Validation section were used for soil properties. These maximum values for wet unit weight, cohesion, and soil internal friction angle were 18.5 kN m^{-3}, 31.3 kN m^{-2}, and 35.7°, respectively. Adhesion and soil-tool friction angle were assumed to be the same as cohesion and soil internal friction angle (i.e., $\delta = \phi$), which was the upper limits of these parameters. Extension of the radial shear zone

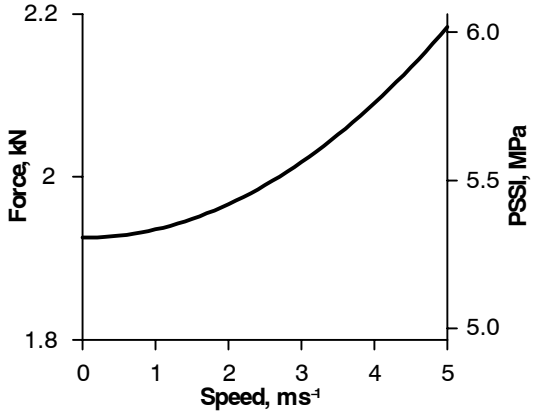

Figure 6. Simulated total force and soil strength on a prismatic tip at a 50 cm depth as a function of operating speed.

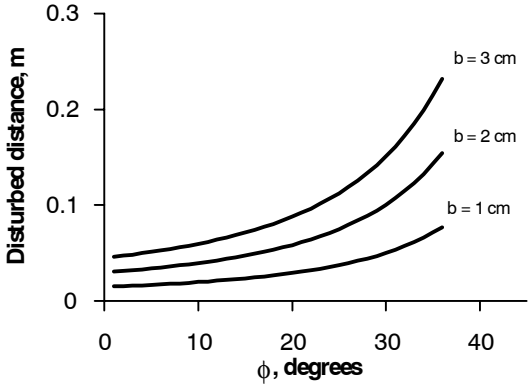

Figure 7. Simulated distance of soil disturbance in the lateral direction for different tool widths and soil internal friction angles.

was set to 45°, as an intermediate value between the minimum (0°) and maximum (90°).

Expected Maximum Soil Strength

Local soil strength at a 50 cm depth was evaluated. Results showed that the force and soil strength (PSSI) experienced by an on-the-go sensor operating horizontally at a depth of 50 cm were less than 2.2 kN and 6.0 MPa at speeds up to 5 m s^{-1} (fig. 6). It should be noted that: (1) extreme values were used for soil properties in the simulation, and (2) the actual operating speed would likely be less than 5 m s^{-1}. Schuring and Emori (1964) defined a critical speed, below which effects of soil inertia would not be significant, as $v = \sqrt{5gb}$, based on the results of dimensional analysis. At the critical speed for the simulated sensor (0.97 m s^{-1}), the increase in soil strength was 0.5% relative to the soil strength at a static condition (i.e., v = 0). Based on these results, selection of a force sensor with a dynamic range greater than 2.2 kN was deemed appropriate.

Distance of Soil Disturbance

From equation 3, the distance of soil disturbance in the lateral direction as a function of tool width and soil internal friction angle for a given cutting angle of the tool is given by:

$$\text{Disturbed distance} = \frac{b}{2}\left[\frac{e^{(\pi-\varepsilon+\phi)\tan\phi}}{\cos\varepsilon}+1\right] \qquad (13)$$

Figure 7 shows the estimated distance of soil disturbance as a function of soil internal friction angle for different tip widths. Tip height was set the same as tip width for this simulation. The simulated distance of soil disturbance would be useful to select locations for sensing tips or prismatic penetrating tools. The spacing between adjacent tips should be greater than the disturbed distance to minimize the interference between tips. For 1, 2, and 3 cm wide tools, the distances of soil disturbance in the lateral direction were 7.7, 15.4, and 23.1 cm, respectively, at the simulated maximum soil internal friction angle (ϕ = 36°). For sensor design, the main concern was interference between the tips in the vertical direction. Soil disturbance in the vertical direction is expected to be less than in the lateral direction due to shape of the prismatic tip, displacing soil mainly to the sides. Although simulation results could give some indication of appropriate tip spacing, the actual amount of interference should be investigated experimentally to determine the final sensor configuration.

PSSI Profile Along Depth

Using equation 4, PSSI was estimated as a function of depth. The operating depth was varied from 1 to 50 cm with a 2 cm increment. The results of the simulation showed that the mechanical resistance acting on the prismatic cutter increased as a squared function of operating speed and as a linear function of operating depth (fig. 8). These theoretical PSSI profiles were obtained with the assumption of homogeneous soil properties within the depth range. Actual PSSI profiles would be more complex and non-linear since soil properties would not be homogeneous along the soil depth. Interpretation of sensor measurements at different depths should consider this increase of PSSI as a function of depth. That is, for identical soil properties, PSSI measured closer to the soil surface will be less than PSSI at greater depths.

Model Validation Using Sensor Field Data

Model validation data were obtained from two research fields in central Missouri, one near Centralia with finer-textured soils, and the other near Hartsburg with coarser-textured soils. Four 10 × 10 m areas were chosen to encompass

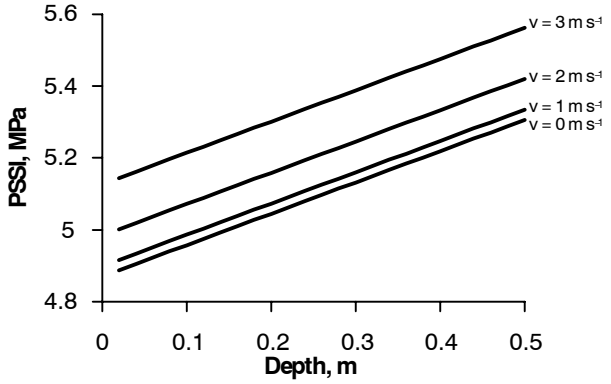

Figure 8. Simulated soil strength (PSSI) at different operating speeds, as a function of operating depth.

Table 2. Properties of soil samples from four 10 × 10 m test areas and validation results of the PSSI and CI models.

Depth (cm)	Soil Unit Weight[a] (kN m^{-3})	Water Content (% d.b.)	Cohesion (kN m^{-2})	Internal Friction Angle (°)	Soil Texture (fraction, decimal)			Measured		Model-Determined			
					Sand	Silt	Clay	PSSI (MPa)	CI (MPa)	PSSI (MPa)	β for PSSI (°)	CI (MPa)	β for CI (°)
Area A													
10[b]	16.6	26.4	20.5	27.8	0.19	0.60	0.21	1.02 (0.27)[c]	0.94 (0.24)	1.02	43.2	0.94	35.6
20	16.5	38.9	25.3	16.2	0.13	0.45	0.43	1.10 (0.15)	1.05 (0.18)	0.78	90.0	0.82	90.0
30	16.2	40.6	20.2	19.9	0.10	0.37	0.54	1.40 (0.18)	0.98 (0.11)	0.92	90.0	0.95	90.0
40	17.2	33.2	18.3	29.5	0.14	0.45	0.41	1.64 (0.24)	1.07 (0.14)	1.64	62.1	1.07	34.9
50	18.2	28.1	26.5	23.3	0.10	0.60	0.30	1.67 (0.73)	1.37 (0.24)	1.67	81.7	1.37	62.1
Area B													
10	16.7	26.5	16.7	33.9	0.12	0.74	0.15	1.53 (1.08)	1.27 (0.33)	1.53	39.5	1.27	29.7
20	18.4	24.3	31.3	29.6	0.13	0.70	0.17	1.65 (0.41)	2.36 (0.37)	1.65	36.1	2.36	50.4
30	18.5	25.2	30.6	35.7	0.11	0.72	0.17	2.43 (0.56)	2.34 (0.46)	2.43	25.0	2.33	20.2
40	18.0	27.3	30.9	27.4	0.22	0.62	0.16	2.51 (0.43)	1.99 (0.52)	2.51	69.7	1.99	51.1
50	16.9	30.2	21.5	32.7	0.14	0.70	0.15	1.55 (0.33)	1.47 (0.40)	1.55	32.1	1.47	22.8
Area C													
10	16.7	14.7	19.6	30.5	0.83	0.13	0.05	0.57 (0.31)	1.28 (0.55)	0.57	4.4	1.28	42.6
20	18.1	21.2	23.7	29.3	0.69	0.25	0.05	0.89 (0.17)	1.71 (0.36)	0.89	20.3	1.70	50.3
30	16.9	21.1	17.4	28.1	0.76	0.17	0.07	1.77 (0.31)	2.26 (0.45)	1.77	77.8	2.26	89.2
40	16.9	23.2	12.0	33.1	0.74	0.17	0.08	1.66 (0.39)	1.85 (0.53)	1.66	58.1	1.85	58.0
50	18.3	27.1	190	32.7	0.47	0.45	0.08	1.00 (0.36)	1.76 (0.44)	1.00	17.3	1.76	35.4
Area D													
10	18.1	24.3	24.3	25.4	0.57	0.25	0.18	0.72 (0.29)	0.56 (0.26)	0.72	28.0	0.56	11.1
20	17.6	25.1	28.7	19.4	0.33	0.45	0.22	0.58 (0.18)	0.65 (0.22)	0.58	32.4	0.65	34.1
30	17.3	31.8	25.0	22.3	0.44	0.30	0.25	1.12 (0.22)	0.96 (0.26)	1.12	69.5	0.96	54.3
40	16.4	30.0	20.2	26.6	0.36	0.41	0.23	1.04 (0.16)	1.08 (0.11)	1.04	49.0	1.08	44.9
50	16.2	32.3	22.1	19.6	0.22	0.61	0.16	0.84 (0.17)	1.13 (0.14)	0.84	72.2	1.13	89.5

[a] Soil weight was calculated by γ = (moist bulk density) × (acceleration of gravity, 9.81 m s^{-2}).
[b] Soil properties corresponding to each sensor depth were determined from 10 cm long samples centered on each depth.
[c] Values in parentheses are standard deviations of field-measured PSSI and CI (MPa).

the texture differences. The two areas selected in the Centralia field included relatively more clay (area A) and relatively more silt (area B) in the soil profile (table 2), while the areas in the Hartsburg field contained relatively more sand (area C) and relatively less sand (area D). PSSIs were collected at five depths (10, 20, 30, 40, and 50 cm) at a nominal operating speed of 1.5 m s^{-1} and a 100 Hz sampling frequency using the prototype SSPS (Chung et al., 2006). Relevant dimensions of the SSPS sensing tips were h = 0.019 m, b = 0.019 m, and α = 60º. From each area, CI profiles were also collected with a 3-probe ASAE-standard small cone penetrometer at 16 to 20 locations. A non-standard penetration rate of 40 mm s^{-1} was used to speed data collection and because our previous research (Sudduth et al., 2004) showed no significant difference in CI between this rate and the standard 30 mm s^{-1}. PSSI and CI measurements were averaged by depth and texture area, resulting in 20 values, one for each depth-area combination. For soil properties, four 7.6 cm diameter, 60 cm deep soil core samples were taken from each area and stored in a cold room at 4°C. Before laboratory tests, the samples were divided into 10 cm long increments corresponding to the five depths at which PSSI data were collected. Soil properties determined from these samples were soil weight and soil water content using gravimetric methods, texture by pipette analysis (Gee and Or, 2002), and cohesion and soil internal friction angle by direct shear tests (Fredlund and Vanapalli, 2002). Data obtained and used in the model validation are summarized in table 2 for those 20 samples (4 areas × 5 depths). Chung (2004) provided more detailed information on sensor construction and data collection.

Strength parameters in table 2 were used as inputs to equations 4 and 12 to determine the optimum extension of the radial shear zone (β) giving soil strength values closest to the field PSSI and CI measurements. Additionally, soil-steel friction angle was calculated by δ = [(0.590 × sand fraction) + (0.735 × silt fraction) + (0.375 × clay fraction)] × ϕ, where the coefficients were interpolated from Potyondy (1961) for unsaturated dense sand, silt, and clay soils, respectively, and adhesion was calculated by ca = c(cotϕ/cotδ), as suggested by Hettiaratchi and Reece (1967). With the variable failure models, the calculated strength values were identical to the measured values, except for two cases where β was constrained at the upper limit of 90°. The value of β determined in the analysis was correlated with soil properties to determine any significant relationships. Visual inspection of scatter plots between the data did not discover any higher-order (nonlinear) relationships. Pearson correlation coefficients of soil properties with β, and significance levels (P values) are summarized in table 3. Pearson correlation coefficients of soil properties to β were significant (P < 0.1) for soil weight, soil water content, internal friction angle, and clay content, except that clay content was not significantly correlated to β for CI (P = 0.16). Soil weight and soil internal friction angle were negatively correlated with β, while soil water content and clay content were positively correlated with β.

When applying our variable failure model, an appropriate value or function for β must be determined. For this validation data, we chose to relate β to measured soil internal friction angle, since this was the measured soil parameter with the

Table 3. Correlations of extension of radial shear zone (β) with soil properties.

	β for PSSI		β for CI	
Soil Property	*r*	P value	*r*	P value
Soil unit weight (kN m^{-3})	–0.40	0.08	–0.48	0.03
Soil water content (%)	0.68	0.01	0.40	0.08
Cohesion (kN m^{-2})	–0.04	0.88	–0.12	0.60
Internal friction angle (ϕ, deg.)	–0.61	0.01	–0.60	0.01
Clay content (decimal)	0.64	0.01	0.33	0.16
Sand content (decimal)	–0.34	0.14	0.02	0.95
Silt content (decimal)	0.02	0.94	–0.23	0.32

largest absolute correlation (table 3) to the model-determined optimum β (table 2) consistent across both PSSI and CI data. Figure 9 shows a scatter plot between the measured soil internal friction angle (ϕ) and the corresponding extension of the radial shear zone (β) determined by the PSSI and CI models. Using linear regression, extension of the radial shear zone was expressed as:

$$\beta = 124.32 - 2.74\phi \ (r^2 = 0.37, P < 0.01) \qquad (14)$$

Then, PSSI and CI were predicted using equations 4 and 12, respectively, by setting β as a function of soil internal friction angle (eq. 14), 0° (Terzaghi, 1943), 90° (Meyerhof, 1951), and ϕ ° (Hu, 1965), and compared with field measured PSSI and CI.

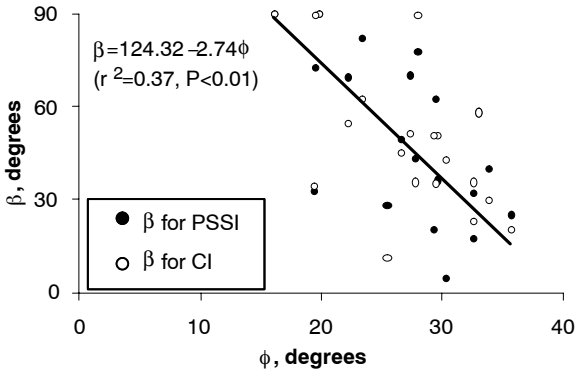

Figure 9. Scatter plot of the optimum extension of the radial shear zone as a function of soil internal friction angle, showing significant negative linear correlations.

Figure 10 shows the results of linear regression (*y*-intercept = 0, α = 0.05) of model-determined soil strength values with different β settings to field PSSI measurements, while figure 11 shows the same relationship for CI measurements. As expected, slopes indicated that Terzaghi's model significantly underpredicted both PSSI and CI measurements, while Meyerhof's model significantly overpredicted measured data. Hu's model showed better predictions of PSSI and CI,

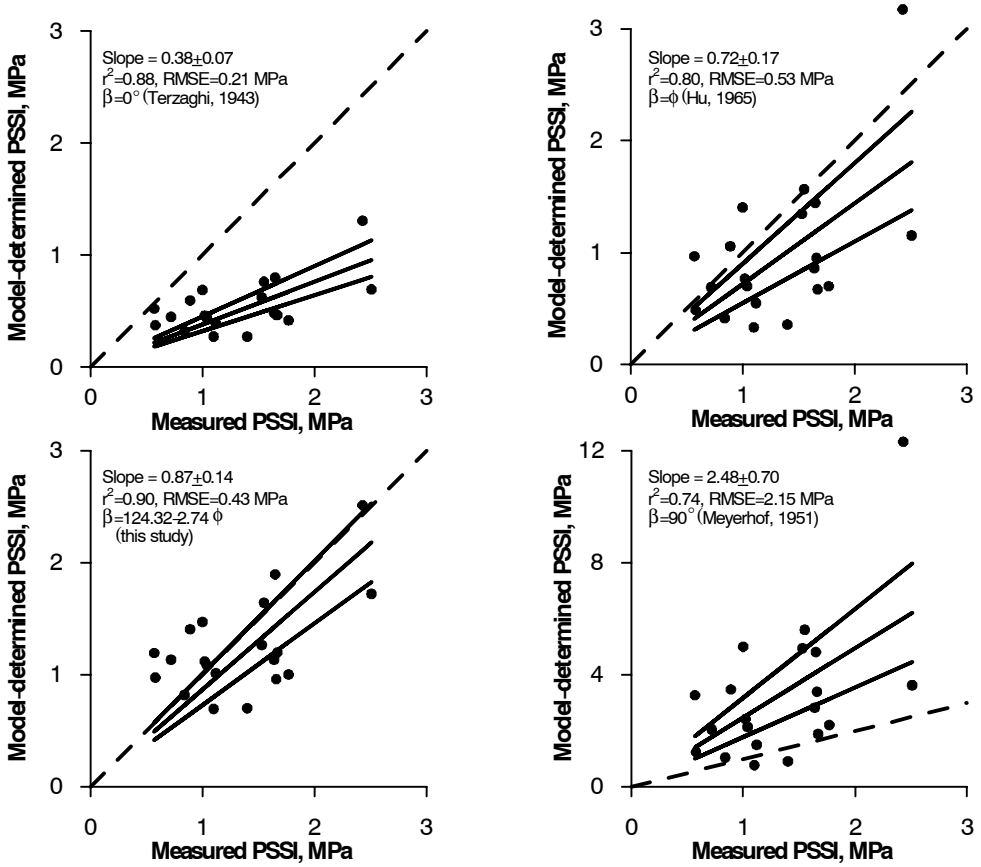

Figure 10. Model-determined soil strength values as a function of field PSSI measurements, using different β values. Individual data points (*n* = 20), linear regression (*y*-intercept = 0), and 95% confidence bands on regression slope are presented, with dashed 1:1 lines shown for comparison.

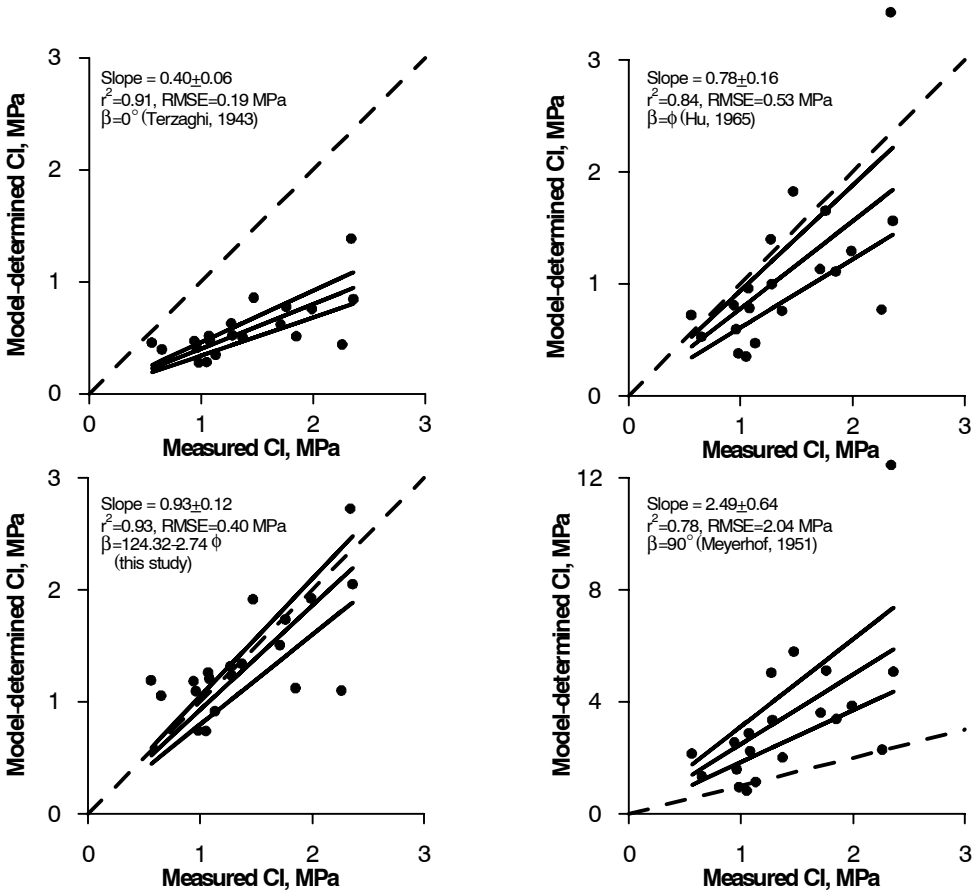

Figure 11. Model-determined soil strength values as a function of field CI measurements, using different β values. Individual data points (n = 20), linear regression (y-intercept = 0), and 95% confidence bands on regression slope are presented, with dashed 1:1 lines shown for comparison.

compared to Terzaghi's and Meyerhof's models, but still significantly underpredicted soil strength measurements. Even though equation 14 only represented 37% of the variability in β, our variable failure model approach exhibited the best prediction of field PSSI and CI measurements, with slopes not significantly different from 1 (α = 0.05).

The variable failure boundary concept is illustrated in figure 12. When a soil has greater internal friction, the failure boundary would extend further in the lateral direction and the extension of the radial shear zone would be less. A soil with lower soil internal friction angle would show the opposite behavior, with less extension of the failure boundary in the lateral direction and greater extension of the radial shear zone. The variable failure boundary relationship developed here (eq. 14) was derived from data representing a wide range in soil properties (table 2) and resulted in reasonable model results (figs. 10 and 11) using a limited dataset. However, additional data collection and modeling would be required to develop a generally applicable expression for estimating the extension of the radial shear zone.

Conclusions

An on-the-go soil strength profile sensor could provide data for estimation of soil compaction. The sensor would obtain measurements comparable to cone index (CI), which has long been used as a standard method, but more rapidly and with a higher spatial density. In this study, soil failure caused by prismatic and conical tools was mathematically modeled and computer-simulated to obtain information useful for on-the-go sensor design and for the interpretation of test results. Major findings are summarized in the following paragraphs.

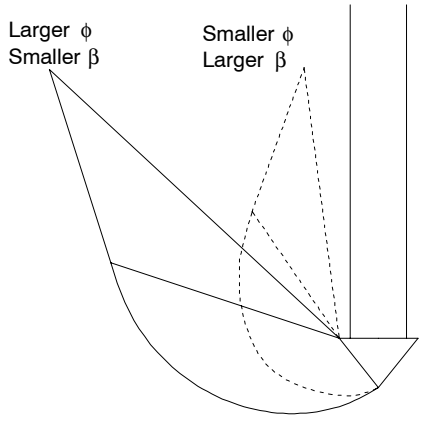

Figure 12. Illustration of the variable failure model concept, exhibiting different extensions of the radial shear zone at different soil internal friction angles.

A model for soil failure caused by a horizontally operating prismatic tool (i.e., soil strength profile sensor) was developed, based on Rankine's passive earth pressure theory. The model was a generalization of previously reported models and used the concept of a variable failure boundary. The model was expressed as an additive function of soil weight, cohesion, adhesion, and operating speed terms. Each term was multiplied by its corresponding dimensionless number, which was a function of tool cutting angle, soil internal friction angle, and soil-metal friction angle.

A model was also developed for soil failure caused by a vertically operating conical tool (i.e., cone penetrometer). Differences between the two models were due to effects of tool geometries (prismatic and conical), and differences in geostatic pressure and soil weight due to the operating directions (horizontal and vertical).

The mathematical models were characterized by examination of the behavior of the dimensionless numbers. For horizontally operating tools, the cohesive component was dominant. However, for vertically operating tools, the gravitational component was also important, especially the effect of soil weight within the failure region. Increases in soil internal friction and soil-metal friction angles resulted in larger dimensionless numbers. Intermediate cutting angles yielding minimum dimensionless numbers were found, and based on this a 60° cutting angle was selected for the sensor design.

Simulation with a 3.61 cm^2 base area for the prismatic tip showed that: (1) the expected force and PSSI acting on the tool were less than 2.2 kN and 6.0 MPa at speeds up to 5 m s^{-1}, (2) the theoretical distance of soil disturbance laterally was 7.7 cm per cm of tip width, and (3) the force acting on the prismatic tool increased as the square of operating speed and linearly with operating depth.

Model validation showed that: (1) good calibrations to mean soil strength were obtained using the variable failure model, (2) the optimum extension of the failure boundary determined from the model was significantly correlated with soil properties including soil weight, soil water content, internal friction angle, and clay content, and (3) when the extension of the failure boundary was expressed as a function of soil internal friction angle, the variable failure model exhibited better predictions of field-measured PSSI and CI than the single failure models developed by previous researchers.

Acknowledgements

This research was supported in part by the North Central Soybean Research Program and the United Soybean Board, USA, and the International Cooperative Research Program, Rural Development Administration, Republic of Korea. The authors appreciate the helpful reviews provided by Prof. Richard J. Godwin and Prof. Mike O'Dogherty, Cranfield University at Silsoe, U.K.

References

Adamchuk, V. I., M. T. Morgan, and H. Sumali. 2001. Application of a strain gauge array to estimate soil mechanical impedance on-the-go. *Trans. ASAE* 44(6): 1377-1383.

Alihamsyah, T., E. G. Humphries, and C. G. Bowers, Jr. 1990. A technique for horizontal measurement of soil mechanical impedance. *Trans. ASAE* 33(1): 73-77.

Andrade, P., U. Rosa, S. K. Upadhyaya, B. M. Jenkins, J. Aguera, and M. Josiah. 2001. Soil profile force measurements using an instrumented tine. ASAE Paper No. 011060. St. Joseph, Mich.: ASAE.

ASAE Standards. 2003a. S313.3: Soil cone penetrometer. St. Joseph, Mich.: ASAE.

ASAE Standards. 2003b. EP542: Procedures for using and reporting data obtained with the soil cone penetrometer. St. Joseph, Mich.: ASAE.

Canarache, A. 1991. Factors and indices regarding excessive compactness of agricultural soils. *Soil and Tillage Res.* 19(2-3): 145-164.

Chukwu, E., and C. G. Bowers. 2005. Instantaneous multiple-depth soil mechanical impedance sensing from a moving vehicle. *Trans. ASAE* 48(3): 885-894.

Chung, S. O. 2004. On-the-go soil strength profile sensor. PhD diss. Columbia, Mo.: University of Missouri.

Chung, S. O., and K. A. Sudduth. 2004. Characterization of cone index and tillage draft data to define design parameters for an on-the-go soil strength profile sensor. *Agric. Biosys. Eng.* 5(1): 10-20.

Chung, S. O., K. A. Sudduth, and J. W. Hummel. 2006. Design and validation of an on-the-go soil strength profile sensor. *Trans. ASABE* 49(1): 5-14.

Fredlund, D. G., and S. K. Vanapalli. 2002. Shear strength of unsaturated soils. In *Methods of Soil Analysis: Part 4. Physical Methods*, 329-361. SSSA Book Series No. 5. J. H. Dane and G. C. Topp, eds. Madison, Wisc.: SSSA.

Gee, G. W., and D. Or. 2002. Particle-size analysis. In *Methods of Soil Analysis: Part 4. Physical Methods*, 255-293. SSSA Book Series No. 5. J. H. Dane and G. C. Topp, eds. Madison, Wisc.: SSSA.

Gill, W. R., and G. E. Vanden Berg. 1968. *Soil Dynamics in Tillage and Traction.* Agricultural Handbook No. 316. Washington, D.C.: USDA Agricultural Research Service.

Glancey, J. L., S. K. Upadhyaya, W. J. Chancellor, and J. W. Rumsey. 1989. An instrumented chisel for the study of soil-tillage dynamics. *Soil and Tillage Res.* 14(1): 1-24.

Godwin, R. J., and G. Spoor. 1977. Soil failure with narrow tines. *J. Agric. Eng. Res.* 22(4): 213-228.

Hettiaratchi, D. R. P., and A. R. Reece. 1967. Symmetrical three-dimensional soil failure. *J. Terramechanics* 4(3): 45-67.

Hettiaratchi, D. R. P., and A. R. Reece. 1974. The calculation of passive soil resistance. *Géotechnique* 24(3): 289-310.

Hettiaratchi, D. R. P., B. D. Witney, and A. R. Reece. 1966. The calculation of passive pressure in two-dimensional soil failure. *J. Agric. Eng. Res.* 11(2): 89-107.

Hillel, D. 1980. *Applications of Soil Physics.* New York, N.Y.: Academic Press.

Hu, G. C. Y. 1965. Bearing capacity of foundations with overburden shear. *Sols Soils* 13: 11-18.

Lambe, T. W., and R. V. Whitman. 1969. *Soil Mechanics.* New York, N.Y.: John Wiley and Sons.

McKyes, E. 1985. *Soil Cutting and Tillage.* Amsterdam, The Netherlands: Elsevier.

McKyes, E., and O. S. Ali. 1977. The cutting of soil by narrow blades. *J. Terramechanics* 14(2): 43-58.

Meyerhof, G. G. 1951. The ultimate bearing capacity of foundations. *Géotechnique* 2(4): 301-332.

O'Callaghan, J. R., and K. M. Farrelly. 1964. Cleavage of soil by tined implements. *J. Agric. Eng. Res.* 9(3): 259-270.

O'Callaghan, J. R., and J. G. McCoy. 1965. The handling of soil by mouldboard ploughs. *J. Agric. Eng. Res.* 10(1): 23-35.

Osman, M. S. 1964. The mechanics of soil cutting blades. *J. Agric. Eng. Res.* 9(4): 313-328.

Payne, P. C. 1956. The relationship between the mechanical properties of soil and the performance of simple cultivation implements. *J. Agric. Eng. Res.* 1(1): 23-50.
Plasse, R., G. S. V. Raghaven, and E. McKyes. 1985. Simulation of narrow blade performance in different soils. *Trans. ASAE* 28(4): 1007-1012.
Potyondy, J. G. 1961. Skin friction between various soils and construction materials. *Géotechnique* 11(4): 339-355.
Reece, A. R. 1965. The fundamental equation of earthmoving mechanics. In *Proc. Symp. Earth-Moving Machines*, Part 3E. London, U.K.: Institute of Mechanical Engineering.
Schuring, D. J., and R. I. Emori. 1964. Soil deforming processes and dimensional analysis. SAE Paper No. 897C. New York, N.Y.: SAE.
Soane, B. D., and C. Van Ouwerkerk. 1995. Implications of soil compaction in crop production for the quality of the environment. *Soil and Tillage Res.* 35(1-2): 5-22.
Stafford, J. V. 1984. Force prediction models for brittle and flow failure of soil by draught tillage tools. *J. Agric. Eng. Res.* 29(1): 51-60.
Sudduth, K. A., J. W. Hummel, and S. T. Drummond. 2004. Comparison of the Veris Profiler 3000 to an ASAE-standard penetrometer. *Applied Eng. in Agric.* 20(5): 535-541.
Terzaghi, K. 1943. *Theoretical Soil Mechanics.* New York, N.Y.: Wiley.
Wismer, R. D., and H. J. Luth. 1972. Performance of plane soil cutting blades in clay. *Trans. ASAE* 15(2): 211-216.

APPENDIX

NORMAL COMPONENT OF THE PASSIVE PRESSURE ACTING ON THE TOOL BASE

In the plane shear zone *aef* (fig. 2), plastic equilibrium requires that along *ae* and *ef* the shearing strength (s_1) is equal to $c + p_1\tan\phi$, where p_1 is the normal pressure expressed by the equation (Meyerhof, 1951):

$$p_1 = \frac{c[\sin(2\eta+\phi)\cos\phi - \sin\phi\cos\phi] + p_0\cos^2\phi}{1-\sin\phi\sin(2\eta+\phi)} \quad \text{(A.1)}$$

In the above equation, p_0 is the pressure acting along *af*. The magnitude of η depends on the degree of mobilization (ranging from 0 to 1) of shearing strength on the surface. Meyerhof (1951) showed that bearing capacity was not very sensitive to the degree of mobilization. Therefore, to simply the analysis, η was set to $\pi/4 - \phi/2$ following the suggestion of Godwin and Spoor (1977). Rearranging equation A.1 then gives:

$$p_1 = c\cos\phi + p_0(1+\sin\phi) \quad \text{(A.2)}$$

Along *ad* the normal and tangential components of the stress on the soil side are (Meyerhof, 1951):

$$p = (s-c)\cot\phi \quad \text{(A.3)}$$

and

$$s = (c + p_1\tan\phi)e^{2\theta\tan\phi} \quad \text{(A.4)}$$

where $\theta = (\pi - \varepsilon) + \beta - \eta = 0.75\pi + 0.5\phi - \varepsilon + \beta$

The corresponding passive pressures on the tool side are:

$$p_p = p = (s-c)\cot\phi \quad \text{(A.5)}$$

and

$$s_p = c_a + p_p\tan\delta \quad \text{(A.6)}$$

From this, the normal component of the passive pressure acting on the tip per unit length of *ad* is:

$$q_n = s_p\sin\varepsilon + p_p\cos\varepsilon \quad \text{(A.7)}$$

Substituting equations A.2 through A.6 into equation A.7 gives the normal component of the passive pressure acting on the tool base:

$$\begin{aligned} q_n &= (s-c)\cot\phi(\cos\varepsilon + \tan\delta\sin\varepsilon) + c_a\sin\varepsilon \\ &= c\left[\frac{\cot\phi\cos(\varepsilon-\delta)}{\cos\delta}\left\{(1+\sin\phi)e^{2\theta\tan\phi} - 1\right\}\right] \\ &\quad + p_0\left[\frac{(1+\sin\phi)\cos(\varepsilon-\delta)}{\cos\delta}e^{2\theta\tan\phi}\right] + c_a\sin\varepsilon \end{aligned} \quad \text{(A.8)}$$